

Testbeam and Laboratory Characterization of CMS 3D Pixel Sensors

M. Bubna^{a*}, E. Alagoz^a, A. Krzywda^a, O. Koybasi^a, K. Arndt^a, D. Bortoletto^a, I. Shipsey^a, G. Bolla^a, A. Kok^l, T.-E. Hansen^l, T. A. Hansen^l, G. U. Jensen^l, J. M. Brom^j, M. Boscardin^b, J. Chramowicz^e, J. Cumalat^f, G. F. Dalla Betta^c, M. Dinardo^h, A. Godshalkⁱ, M. Jones^a, M. D. Krohn^f, A. Kumarⁱ, C. M. Lei^e, L. Moroni^g, L. Perera^f, M. Povoli^c, A. Prosser^e, R. Rivera^e, A. Solano^d, M. M. Obertino^d, S. Kwan^e, L. Uplegger^e, C. D. Via^m, L. Vigani^g, S. Wagner^f

^a *Physics Department, Purdue University, West Lafayette, IN 47907-2036, USA*

^b *Centro per i Materiali e i Microsistemi Fondazione Bruno Kessler (FBK), Trento, Via Sommarive 18, I-38123 Povo di Trento (TN), Italy*

^c *INFN Padova (Gruppo Collegato di Trento) and Dipartimento di Ingegneria e Scienza dell'Informazione, Universita di Trento, Via Sommarive 14, I-38123 Povo di Trento (TN), Italy*

^d *INFN Torino, Italy*

^e *Fermilab, Batavia, IL 60510-5011, USA*

^f *University of Colorado at Boulder, Boulder, CO, USA*

^g *INFN Milano-Bicocca, Milan, Italy*

^h *Universita and INFN, Milano-Bicocca, Italy*

ⁱ *SUNY, Buffalo*

^j *Institut Pluridisciplinaire Hubert Curien (IPHC)-Inst. Nat. Phys)*

^k *University of Mississippi (US)*

^l *SINTEF, Sintef MiNaLab, Blindern, 0314 Oslo, Norway*

^m *Particle Physics group, University of Manchester, M139PL Manchester, UK*
E-mail: mbubna@purdue.edu

ABSTRACT: The pixel detector is the innermost tracking device in CMS, reconstructing interaction vertices and charged particle trajectories. The sensors located in the innermost layers of the pixel detector must be upgraded for the ten-fold increase in luminosity expected with the High-Luminosity LHC (HL-LHC) phase. As a possible replacement for planar sensors, 3D silicon technology is under consideration due to its good performance after high radiation fluence. In this paper, we report on pre- and post- irradiation measurements for CMS 3D pixel sensors with different electrode configurations. The effects of irradiation on electrical properties, charge collection efficiency, and position resolution of 3D sensors are discussed. Measurements of various test structures for monitoring the fabrication process and studying the bulk and surface properties, such as MOS capacitors, planar and gate-controlled diodes are also presented.

KEYWORDS: CMS; Pixel; Phase 2 upgrade; HL-LHC; 3D sensors; Silicon.

*Corresponding author.

Contents

1. Introduction	1
2. Electrical characterization	3
2.1 Post-irradiation IV measurements	4
3. Laboratory Measurements	5
3.1 Noise before and after irradiation	5
3.2 Charge before and after irradiation	5
4. Testbeam Measurements	6
4.1 Pre-irradiation efficiency	7
4.2 Efficiency vs. threshold and bias	7
4.3 Post-irradiation efficiency	8
5. Measurement of Test Structures	9
6. Conclusions and Outlook	9

1. Introduction

The current CMS pixel detector [1] can operate up to a fluence of $6 \times 10^{14} \text{ n}_{\text{eq}}/\text{cm}^2$. New rad-hard sensor candidates are required for High Luminosity LHC or HL-LHC, which will increase the design luminosity fifty times to $L = 5 \times 10^{34} \text{ cm}^{-2}\text{s}^{-1}$ [2]. The new detector will be exposed to a dose of $10^{16} \text{ n}_{\text{eq}}/\text{cm}^2$ at a radii of 5 cm from the interaction point during the operation of HL-LHC. This is ten times higher than the design fluence of the current detector [3]. Current CMS pixel sensors have already shown serious performance degradation at a fluence of $10^{15} \text{ n}_{\text{eq}}/\text{cm}^2$ [4], demonstrating that the pixel detector will not withstand higher radiation doses. One of the major candidates for replacing the current planar technology is 3D silicon sensors [5]. In 3D detectors, p+ and n+ electrodes are composed of arrays of columns ($r \sim 5\text{-}14 \mu\text{m}$) which penetrate into the bulk of the detector. Lateral depletion and smaller electrode spacing causes: (a) smaller carrier drift distance which leads to faster charge collection, (b) lower depletion voltage, (c) small trapping probability after irradiation, which leads to superior radiation hardness, and (d) allows implementation of Active Edge concept which reduces dead region on the edge of the detectors. The smaller electrode spacing in 3D detectors leads to higher capacitance, which increases the sensor noise and degrades the Signal to Noise (S/N) ratio. 3D detectors also require complex processing which is now getting standardized every day at various research institutes (Stanford, FBK, Sintef, CNM).

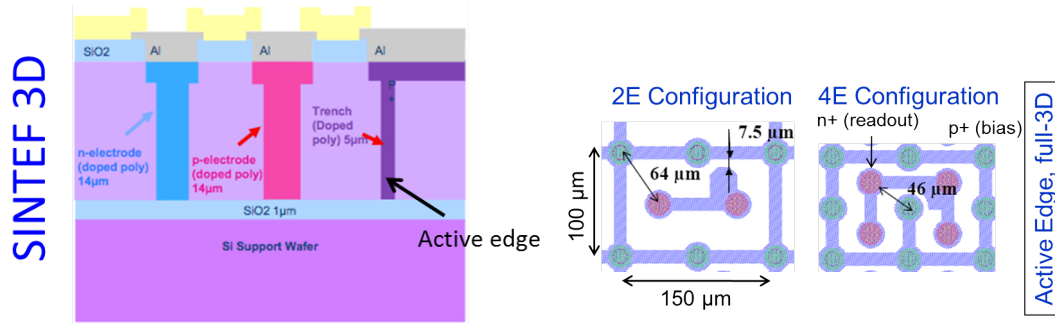


Figure 1. Wafer cross-section (left) and pixel layout (right) of Sintef 3D 2E and 4E sensors

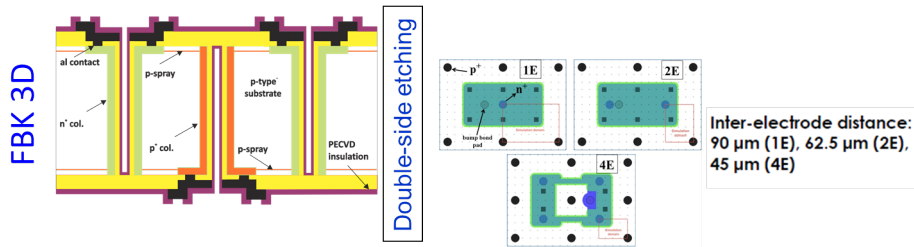


Figure 2. Wafer cross-section (left) and pixel layout (right) of FBK 1E, 2E and 4E sensors.

In order to reduce the costs and improve yield, Fondazione Bruno Kessler (FBK), Trento, Italy [6], and Centro Nacional de Microelectronica (CNM-IMB), Barcelona, Spain [7], have independently developed the so-called 3D Double-side Double-Type Column (3D-DDTC) sensors. These designs offer advantages in terms of process complexity with respect to the original Full 3D sensor technology. The 3D collaboration has been extended to include SINTEF (Norway) [9] which is committed to the small-to-medium scale production of Active Edge, Full-3D silicon sensors. The intrinsic feature of the SINTEF 3D detector is that it can be fabricated with an active edge, so that the width of the inactive periphery can be reduced to only a few microns. Figure 1 and 2 show the cross-section and pixel sensor layout of 3D pixel sensors, manufactured at Sintef and FBK respectively.

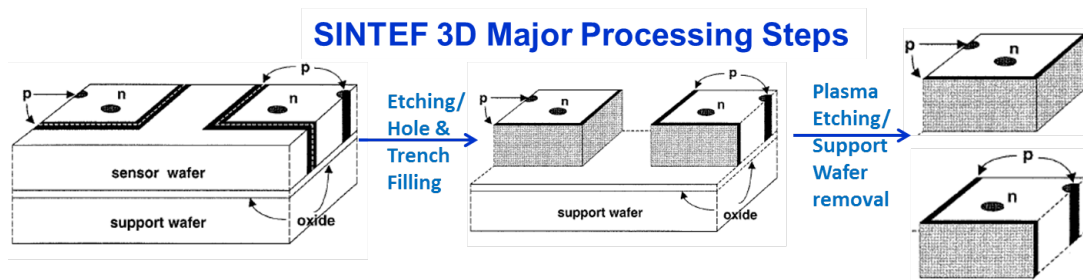


Figure 3. Support wafer removal to get Active edge 3D sensors using new WaferBOND© process from Brewer Science

The sensors considered in this study are 3D pixel sensors from the FBK Double-side Double-type Column (3D-DDTC) ATLAS08, ATLAS11 and ATLAS12 batches (all 200μm thickness). We

also present results for Sintef 3D pixel sensors (200 μm and 285 μm bulk thickness) which have an active edge of $\sim 5\mu\text{m}$. The sensors were bump-bonded to the CMS PSI46v2 Read-out Chip. The support wafer of 500 μm thickness in Sintef wafers was recently removed by plasma etching, using the new WaferBOND[®] process from Brewer Science. Figure 3 shows the various steps involved in removal of support wafer of Sintef 3D wafers. We also present characterization results for various test structures (Planar diodes, MOS Capacitors) and 1E diodes from ATLAS10 batch. The CMS 1E 3D diodes from ATLAS10 batch are made from a p-type material with a thickness of 200 μm and consists of a 19x29 pixel array [11].

The sensors were irradiated at the Los Alamos LANCSE facility with 800 MeV protons to fluences in the range of $7 \times 10^{14} \text{ n}_{\text{eq}}/\text{cm}^2$ to $3.5 \times 10^{15} \text{ n}_{\text{eq}}/\text{cm}^2$. Also, the 3D diodes from ATLAS10 were irradiated with Co^{60} gamma source to a dose of 2.2 MRad. The 3D diodes were actively biased during irradiation. Some of the post-irradiation measurement results for FBK 3D sensors from ATLAS08 and ATLAS10 1E diodes were presented earlier in [12].

2. Electrical characterization

Leakage current is the major quality control factor of any fabrication process. FBK 3D pixel sensors were characterized in the laboratory at room temperature before irradiation. The measured leakage currents as a function of the bias voltage are shown in Figure 4 for ATLAS08, ATLAS11 and ATLAS12 batch sensors. FBK ATLAS08 sensors had very high inter-pixel isolation (using p-spray) which caused unusually low breakdown [10]. The p-spray doping was reduced in ATLAS10 and later batches, which improved the breakdown voltage behavior. FBK ATLAS11 and ATLAS12 1E sensors from IBL batches show depletion voltage of $\sim 5\text{-}10\text{V}$, leakage current of $10\text{-}200 \text{ nA}$ for 1E sensors and a breakdown voltage of $35\text{V-}45\text{V}$. Compared to leakage current in current planar sensors in CMS ($10\text{-}100 \text{ nA}$), electrical performance is quite good. Leakage current determines the amount of power needed to operate the detector, especially after irradiation.

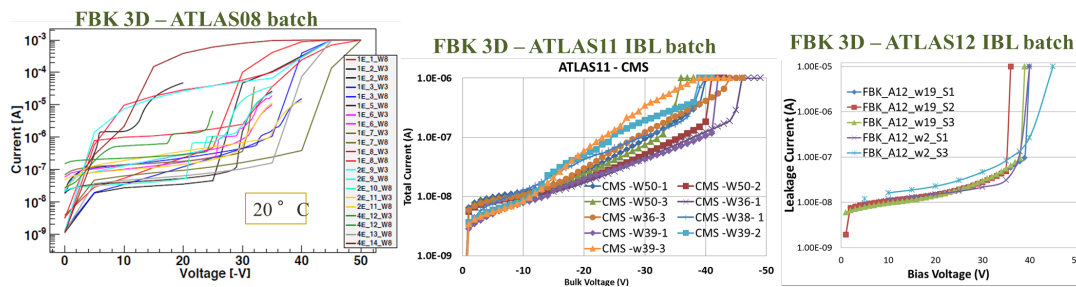


Figure 4. IV curves of FBK 3D pixel sensors before irradiation at 20°C from ATLAS08 batch (left), ATLAS11 batch (middle) and ATLAS12 batch (right)

Figure 5 shows the leakage current results for Sintef 2E and 4E sensors, with and without support wafer. Ideally, 2E sensors will have lower breakdown voltage due to smaller inter-electrode spacing and higher electric fields. The leakage current is slightly higher ($200 \text{ nA-}4\mu\text{A}$) for Sintef sensors with support wafer. The sensors get fully depleted at $\sim 10\text{V}$ and breakdown voltage is 100V for 2E and $120\text{V-}140\text{V}$ for 4E sensors. After removing the support wafer, leakage for 2E is

very good (5nA), while it is comparable to planar sensors for 4E sensors (150nA). Depletion and breakdown voltages are similar to sensors with support wafer.

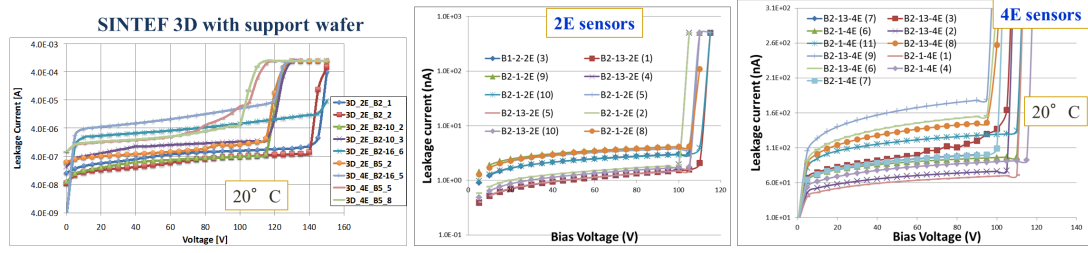


Figure 5. IV curves of Sintef 3D sensors with support wafer (left) and after support wafer removal for 2E sensors (middle) and 4E sensors (right)

2.1 Post-irradiation IV measurements

Figure 6 shows the leakage current after irradiation measured for different sensors. FBK ATLAS08 sensors were measured at -20°C after 7×10^{14} - 3.5×10^{15} n_{eq}/cm^2 proton irradiation. FBK ATLAS08 sensors have strange behavior which is caused by fabrication defects and radiation induced traps. FBK ATLAS10 diodes (after 2.2 Mrad Co⁶⁰ gamma irradiation) show increase in breakdown from 40V to 80V after irradiation. Since gamma irradiation mostly affects the surface behavior of the devices, the increase in leakage current is relatively small. The improvement in breakdown voltage is related to improved interface carrier concentration and better surface mobility which leads to higher breakdown voltage.

For Sintef 3D sensors after irradiation, the leakage current increases to 500nA - 5 μ A at -30°C. The breakdown voltage degrades after irradiation and ranges from 50V to >160V after irradiation. Leakage current has a non-flat slope in many sensors after irradiation which is due to radiation induced traps. For highest dose Sintef 3D sensor (3.5×10^{15} n_{eq}/cm^2), it was difficult to measure leakage current due to thermal runaway. In order to recover the charge loss after irradiation due to trapping, higher bias voltage needs to be applied to the sensor. Thus, lower breakdown voltage after irradiation, especially for ATLAS08 sensors, reduces the amount of charge which can be collected after irradiation.

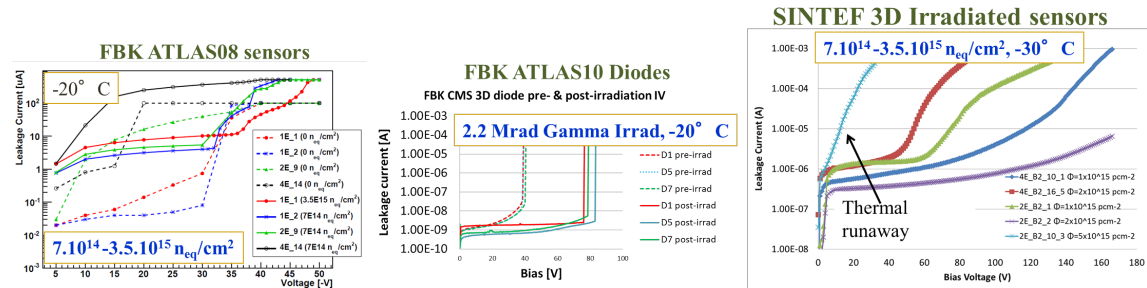


Figure 6. IV curve of FBK 3D ATLAS08 sensors, ATLAS10 1E diodes before and after 2.2 Mrad Co⁶⁰ gamma irradiation, and SINTEF 3D sensors after 3.5×10^{15} n_{eq}/cm^2

3. Laboratory Measurements

Sensors were tested with a 1mCi Sr^{90} radioactive source for lab measurements. PSI testboard and psi46expert software were used as DAQ system. Random trigger generated by DAQ system was used to collect data from source. The hit timestamp in ROC buffer was compared with trigger generated by DAQ system.

3.1 Noise before and after irradiation

S-curve test was used to determine the pixel noise by sending internal calibration signals through the injection capacitor to the ROC preamplifier input and measuring the response efficiency on a pixel-by-pixel basis. Noise measurements are taken at room temperature before irradiation, and at -20°C after irradiation. The tests are based on single measurements, with no averaging of S-curve results. Figure 7 (left) shows the simulated $C - V$ and $1/C^2 - V$ results for FBK 1E, 2E and 4E sensors ($200\mu\text{m}$ thickness). Higher number of electrodes leads to larger capacitance, and larger noise.

Figure 7 (middle) and (right) shows the measured noise before and after irradiation for FBK and Sintef 3D sensors respectively. Before irradiation, 2E sensors ($220e^-$ - $280e^-$) are $\sim 2\times$ noisier and 4E sensors ($360e^-$ - $450e^-$) are $\sim 4\times$ noisier compared to 1E and planar sensors ($100e^-$ - $150e^-$). Capacitance (and thus noise) increases with radiation damage and smaller electrode spacing, but decreases with reverse bias. The increase after radiation ($50e^-$ - $100e^-$) is mainly due to increased shot noise caused by increased leakage current.

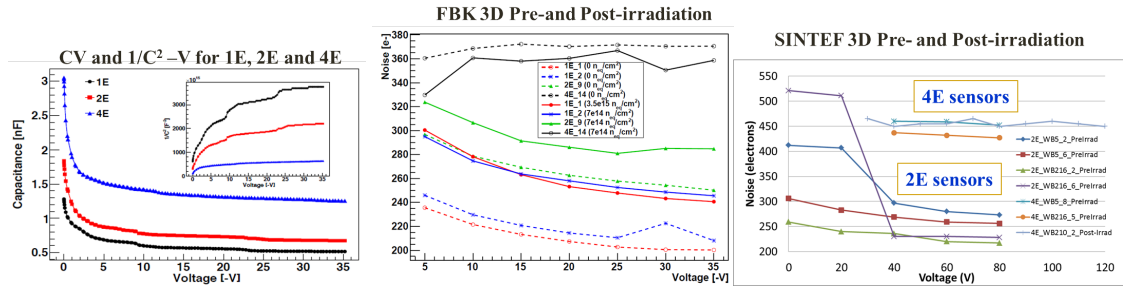


Figure 7. Noise of: FBK 3D ATLAS08 sensors simulation results (left), pre-irradiation and post-irradiation ATLAS08 (middle), and SINTEF 3D sensors (right) before and after $3.5 \times 10^{15} \text{ n}_{\text{eq}}/\text{cm}^2$ irradiation

3.2 Charge before and after irradiation

Figure 8 shows the charge collected with a Sr^{90} source before and after irradiation for Sintef 3D sensors. The sensors were biased at -80V for 2E sensors, and at -100V for 4E sensors, and a threshold of 3900 electrons was set. The collected charge before irradiation was 17 - 19.4 ke^- for a 2E and 16.9 ke^- for a 4E sensor (all $285 \mu\text{m}$ thickness). There are differences between measured and expected values (18.5 ke^-) of collected charge. This is mainly due to charge sharing and wafer thickness uncertainty. Another possible factor in the mismatch of collected charge is due to secondary electrons created by scattering from support wafer which explains the abnormally high charge collected in some 2E sensors.

After $3.5 \times 10^{15} \text{ n}_{\text{eq}}/\text{cm}^2$, the CMS pixel readout chip survived in only one Sintef 2E module (irradiated to lowest dose of $7 \times 10^{14} \text{ n}_{\text{eq}}/\text{cm}^2$). The current CMS pixel readout chip was designed for a fluence of $6 \times 10^{14} \text{ n}_{\text{eq}}/\text{cm}^2$ only, so most of the ROCs died after irradiation. The charge collected in irradiated Sintef 2E was 12.9 ke^- which is a loss of 23%. In FBK ATLAS08 sensors, charge loss was 14% in both 2E and 4E sensors after $7 \times 10^{14} \text{ n}_{\text{eq}}/\text{cm}^2$. For comparison, the signal loss in CMS planar pixels is about 50% after $10^{15} \text{ n}_{\text{eq}}/\text{cm}^2$ at 600V [3], [4]. Thus, 3D sensors show promising results compared to planar sensors.

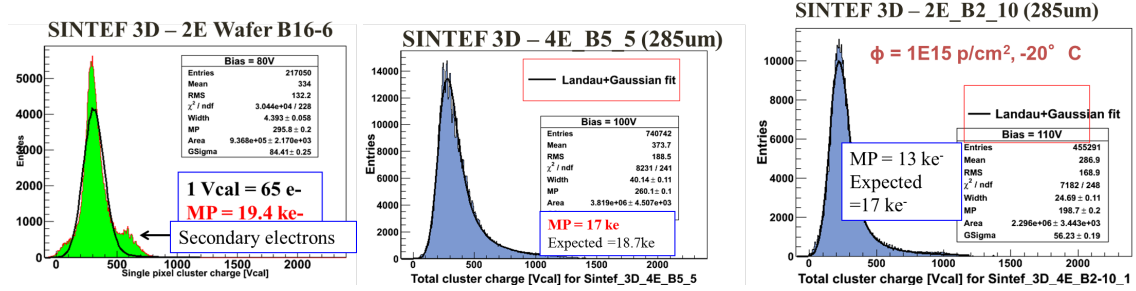


Figure 8. Charge collected from source for Sintef 2E before irradiation (left), Sintef 4E before (middle) and (right) after $7 \times 10^{14} \text{ n}_{\text{eq}}/\text{cm}^2$ irradiation

By combining the charge collected and measured noise results, Signal-to-Noise (S/N) ratio for FBK ATLAS08 and Sintef 3D sensors can be calculated. Table 1 shows the S/N ratio for 1E sensors is highest before irradiation, but after irradiation 2E sensors have the best S/N ratio. This is due to the increased noise in 4E sensors due to large capacitance (pre-irradiation) and large shot noise due to increased leakage current (post-irradiation).

FBK ATLAS08 3D	S/N Pre-irrad	S/N Post-irrad
1E	66	33
2E	46	38
4E	36	32
Sintef 3D	S/N Pre-irrad	S/N Post-irrad
2E	60	28
4E	40	X

Table 1. Signal-to-Noise (S/N) ratio for different FBK and Sintef 3D sensors before and after irradiation.

4. Testbeam Measurements

Sensors were tested with 120 GeV/c protons at the Fermilab Meson Test Facility. The Fermilab testbeam setup is described in [8]. A telescope made of eight planes of planar CMS pixel detectors was used to reconstruct the tracks. The intrinsic track resolution is about $7 \mu\text{m}$ in both the X and Y local coordinates. The trigger signal is provided by two PMTs coupled to scintillators, downstream from the telescope. No magnetic field is applied. DUTs are tilted to various angles with respect

to the beam to improve resolution. Event data from the test beam is analyzed using alignment software developed at INFN Milano, Italy specifically for the Fermilab test beam.

4.1 Pre-irradiation efficiency

Figure 9 shows the cell efficiency for Sintef 2E and 4E pixel sensors after support wafer removal. An event's efficiency is equal to one if a hit is registered within one pixel width of a reconstructed track, and zero otherwise. Only events with one track are considered. The total sensor efficiency is determined by averaging the efficiency of all the events in a run.

The efficiency was measured at different bias voltages (see Section 4.2) and at different angles. Figure 9 (left) shows the efficiency of a single Sintef 2E pixel, reconstructed from all the tracks information. The sensor was biased at -100V with the detector orthogonal to the beam (angle of 0°). The maximum cell efficiency was 94%. The efficiency increases by rotating the DUT on short pitch with respect to the beam axis, reaching a value of 98.7% for 2E and 97.5% for 4E (Figure 9 (right)) at angle of 20° . The small decrease in full efficiency (100%) is partially explained by the bias and readout electrodes in the bulk, being inactive volumes for tracks impinging orthogonal to the detector. This is shown in Figures 1 and 2 where readout columns corresponding to the n+ columns in the middle of the sensor and the six p+ electrodes corresponding to bias columns on the edges are visible.

Similar results were found for FBK ATLAS11 and ATLAS12 sensors. The maximum cell efficiency for ATLAS12 sensor was found to be 97.3% after rotation.

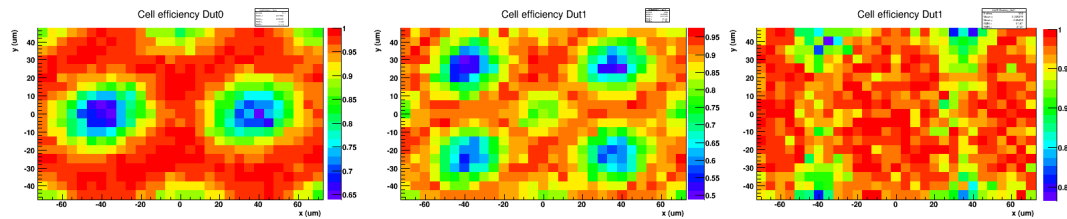


Figure 9. Cell efficiency of (left) Sintef 3D 2E sensors at 0 degree, 4E sensors at 0 degree (middle) and 4E at 20 degrees (right)

4.2 Efficiency vs. threshold and bias

In order to find the best threshold and bias values for sensor operation, efficiency values are measured at different threshold and bias values. Figure 10 shows the efficiency for various FBK and Sintef 3D pixel sensors as a function of threshold (left) and reverse bias (right). $V_{thrComp}=125$ ADC corresponds roughly to an absolute threshold of $3.9ke^-$. In Figure 10 (left), absolute chip threshold is inversely proportional to $V_{thrComp}$ as shown in ADC units; as $V_{thrComp}$ ADC increases, absolute threshold decreases. Thus, sensor efficiency falls off at lower absolute threshold (higher ADC values). For Sintef 2E, threshold increased by $\sim 2ke^-$ after irradiation. This is due to several factors: (a) shift in threshold voltage of transistors in the Readout chip which slows the chip operation and increases threshold due to timewalk, and (b) degradation in sensor performance causing increased noise (shot noise due to leakage).

Efficiency increases with sensor reverse bias voltage due to larger electric fields in the bulk, up to the breakdown voltage after which it falls off. Figure 10 (right) shows that the efficiency for both

FBK and Sintef 3D sensors is roughly constant as they are operated well above the full depletion voltage of the sensors. Radiation damage has a significant effect on efficiency far away from the readout electrodes in 3D sensors.

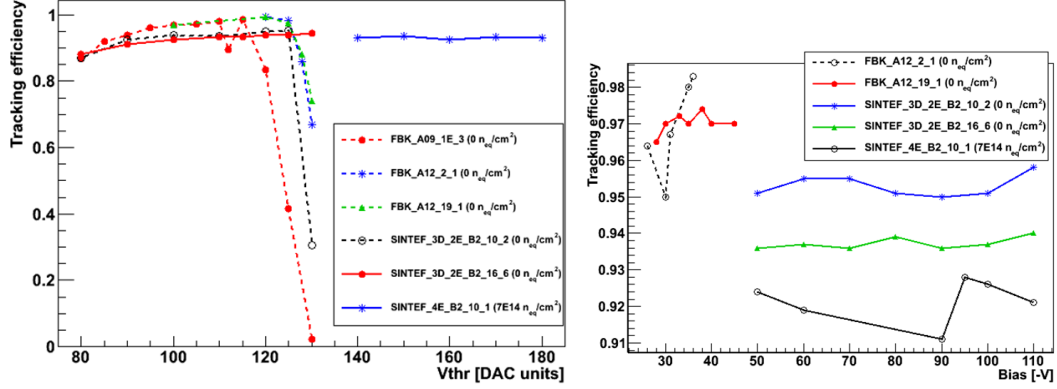


Figure 10. Tracking efficiency of FBK and Sintef 3D sensors as a function of (a) Vthr ADC (left) and (b) sensor reverse bias (right)

4.3 Post-irradiation efficiency

Figure 11 shows the efficiency for an individual Sintef 2E pixel after irradiation with 7×10^{14} n_{eq}/cm² protons. The efficiency of the sensor reduced to 94.5% as shown in Figure 11 (left) after irradiation. By rotating the sensor to 20° on long pitch, cell efficiency was improved to 96.5% after irradiation. Table 2 shows the cell efficiency for various 3D sensors before and after irradiation. For FBK ATLAS08 batch, 2E sensors have the least loss in efficiency after irradiation. For Sintef 3D, readout chip in only one 2E module survived after irradiation. The unusually low drop in efficiency for Sintef 2E sensor after irradiation may indicate anomalous irradiation dose and needs to be investigated further.

Track residuals are calculated as the distance between the predicted and measured positions of a cluster, in either the local X or Y direction. The residuals are fitted with a Gaussian distribution: the overall sensor resolution is determined from the sigma of the fit. Best post-irradiation residual of $12.56 \mu\text{m}$ was measured for a FBK 2E sensor from ATLAS08 batch. Track residual of $8.5 \mu\text{m}$ was measured for Sintef 2E before irradiation (Figure 11 (middle)) and $9.2 \mu\text{m}$ after irradiation (Figure 11 (right)).

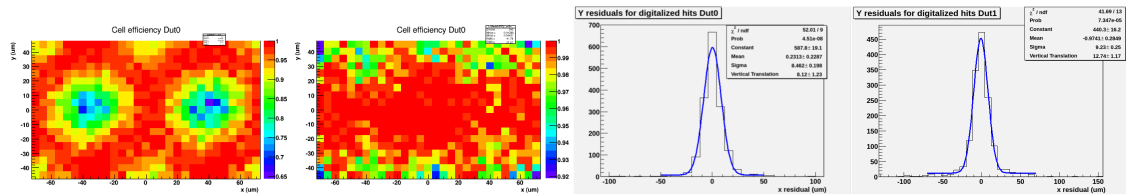


Figure 11. Cell efficiency of Sintef 3D 2E sensors after irradiation (left) at 0 degrees and 20 degrees, residual of Sintef 2E sensor before (middle) and after irradiation(right)

Sensor type	Maximum Efficiency	Loss in Efficiency after irradiation
Efficiency before irradiation		
FBK ATLAS08 1E_1	97.8%	-
FBK ATLAS08 1E_2	97.6%	-
FBK ATLAS08 2E_9	95.4%	-
FBK ATLAS08 4E_12	94.5%	-
FBK ATLAS12 ATLAS12_1E	97.3%	-
SINTEF 3D 2E	98.7%	-
SINTEF 3D 4E	97.5%	-
Efficiency after irradiation with 7×10^{14} n_{eq}/cm² protons		
FBK ATLAS08 1E_1(3.5E15)	37.9%	59.9%
FBK ATLAS08 1E_2(7E14)	73.1%	25%
FBK ATLAS08 2E_9(7E14)	91.1%	4%
FBK ATLAS08 4E_14(7E14)	81.7%	13%
SINTEF 3D 2E (7E14)	96.5%	1.2%

Table 2. Cell efficiency for various FBK and Sintef 3D sensors, before and after irradiation

5. Measurement of Test Structures

The electrical and tracking properties of pixel sensors depend on material properties of bulk silicon and its interface with silicon dioxide. For example, interface traps between the sensor and Silicon oxide affects surface current before irradiation and sensor's post-irradiation p-stop performance. The density of fixed oxide charges affects depletion voltage, noise and gain of readout chip. In order to better understand bulk and interface properties of silicon sensors and their effects on sensor properties, various test structures for FBK ATLAS10 and later batches were measured and their material parameters were calculated. Figure 12 (left) shows some of these structures: MOS and planar capacitors, planar and 3D diodes, gate controlled diodes. The measurements include IV measurements, quasi-static and high frequency CV measurements. Figure 12 (middle) shows the low-frequency (1-2 Hz) and high-frequency (1kHz) CV measurements and Figure 12 (right) the density of interface traps measured for ATLAS10 sensors. The density of interface traps measured was 7.6×10^8 - 8.9×10^9 traps/cm³. This value is comparable to the ideal value of 10^8 - 10^{10} traps/cm³. Similarly, by measuring IV and CV of planar diodes and combining the results, generation lifetime of electrons and holes was measured as $\tau_{g1} = 5.78ms$ and $\tau_{g2} = 3.64ms$. Generation and recombination lifetimes help to understand leakage and charge collection results.

6. Conclusions and Outlook

This paper presented results on 3D sensor designs from different vendors. 3D sensors offer several improvements over planar sensors, especially at higher luminosities. 3D sensors show good charge collection results, both before and after irradiation. 3D sensors also have good tracking efficiency and spatial resolution, but suffer from higher noise compared to planar sensors. The reduced efficiencies after irradiation arises due to higher readout threshold and low electric field. After irra-

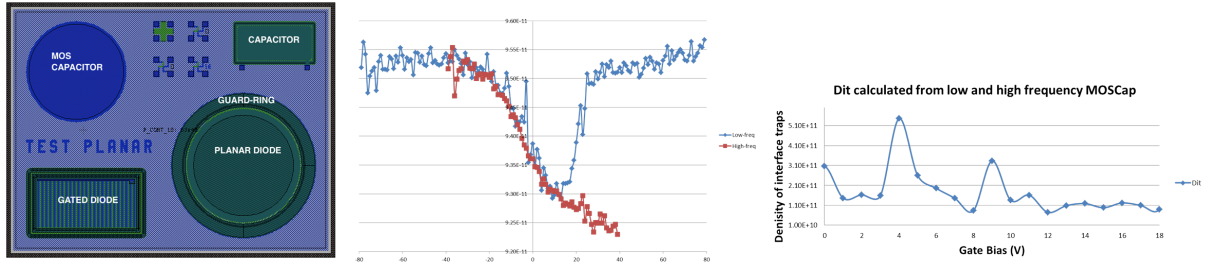


Figure 12. Various test structures (left) from FBK ATLAS10 batch, low and high frequency CV of MOS capacitor, and (right) measured density of interface traps

diation, 2E showed the greatest efficiency and charge collection for FBK sensors. 2E sensors also offers best S/N ratio while providing good tracking efficiency and resolution.

More work needs to be done to reach radiation hardness of 10^{16} neq/cm² and the performance needed for HL-LHC. TCAD Simulation efforts are on-going to understand FBK and Sintef sensor laboratory and beam test results. By going to smaller and thinner pixels, tracking efficiency and resolution uncertainty can be improved. Using digital readout chip with lower threshold will help to improve charge collection efficiency after irradiation. Technology improvements also need to be made in order to aggressively improve 3D inter-electrode spacing for improved radiation tolerance.

References

- [1] D. Bortoletto et al., The CMS pixel system, Nucl. Instr. and Meth. A 579 (2007) 669.
- [2] The HiLumi LHC Design Study website, <http://hilumilhc.web.cern.ch/hilumilhc/index.html>
- [3] G. Auzinger et al., Silicon sensor development for the CMS tracker upgrade, 2011 JINST 6 P10010.
- [4] T. Rohe et al., Radiation hardness of CMS pixel barrel modules, Nucl. Instr. and Meth. A 612 (2010) 493.
- [5] S. I. Parker et al., 3D - A proposed new architecture for solid-state radiation detector, Nucl. Instr. and Meth. A 395 (1997) 328.
- [6] A. Zoboli et al., Double-Sided, Double-Type-Column 3-D Detectors: Design, Fabrication, and Technology Evaluation, IEEE Trans. Nucl. Sc. NS-55 (5) (2008) 2775.
- [7] G. Pellegrini et al., First double-sided 3-D detectors fabricated at CNM-IMB, Nuclear Instruments and Methods in Physics Research Section A592 (2008) 38.
- [8] L. Uplegger et al., Test-beam studies of diamond sensors for SLHC, in press, doi:10.1016/j.nima.2012.11.076
- [9] O. Koybasi et al., Assembly and qualification procedures of CMS forward pixel detector modules, Nucl. Instr. and Meth. A 638 (2011) 55.
- [10] E. Alagoz et al., Simulation and laboratory test results of 3D CMS pixel detectors for HL-LHC, 2012, JINST 7 P08023
- [11] M. Povoli et al., Impact of the layout on the electrical characteristics of double-sided silicon 3D sensors fabricated at FBK, 2012, JINST 7 P08023
- [12] M. Bubna et al., Testbeam and laboratory test results of irradiated 3D CMS pixel detectors, Nucl. Instr. and Meth. A, 732 (2013) 52-56.